NANO · MICRO small
www.small-journal.com

Harnessing *Lactobacillus reuteri*-Derived Extracellular Vesicles for Multifaceted Cancer Treatment

Soyeon Yi, Eunkyeong Jung, Hyeran Kim, Jinsol Choi, Suhyeon Kim, Eun-Kyung Lim, Kwang-Sun Kim, Taejoon Kang, and Juyeon Jung**

Extracellular vesicles (EVs) have emerged as valuable biological materials for treating intractable diseases. Extensive studies are conducted on EVs derived from various cellular sources. In this study, EVs derived from *Lactobacillus reuteri* (*L. reuteri*), a probiotic, exhibit remarkable cancer therapeutic efficacy when administered orally is reported. These *L. reuteri*-derived EVs (REVs) demonstrate stability in the gastrointestinal tract and exert significant anti-tumor effects. Using A549 cells and murine models, we confirmed that REVs mediate their therapeutic effects by modulating apoptotic signaling pathways. Furthermore, the combination of REV with drugs enhances tumor ablation and induces immunogenic cell death. In a mouse model, oral administration of REVs encapsulating indocyanine green followed by photothermal therapy led to complete tumor elimination within 32 days. REVs represent a promising biological therapeutic platform for cancer treatment, either independently or in combination with other therapies, depending on the treatment objectives.

1. Introduction

Extracellular vesicles (EVs) are nano-sized, membrane-bound particles released by cells into the extracellular environment, containing biological materials such as proteins, nucleic acids, and lipids.[1,2] The properties of EVs vary considerably depending on their cellular origin and the physiological or pathological conditions under which they are produced.[3] This variability has led to the use of EVs in a variety of applications. EVs play pivotal roles in various biological processes, including cell-to-cell communication, immune regulation, and tissue homeostasis.[4] Consequently, research into their medical applications has expanded significantly. EVs are particularly promising for disease treatment due to their ability to mimic the properties of their source cells and their potential for engineering to enable drug delivery. For example, EVs derived from immune cells such as natural killer cells exert potent anti-tumor effects by modulating immune responses against cancer cells.[5] These effects can be further enhanced by loading EVs with therapeutic substances such as cytokines to improve tumor targeting and treatment efficacy.

Probiotic-derived EVs retain many of the beneficial properties of their parent cells and show potential for cancer treatment.[6] Current strategies include modulating the gut microbiota to enhance immune responses, exerting direct anti-tumor effects, and achieving synergistic outcomes when used in combination with conventional therapies. For instance, some probiotics produce metabolites that inhibit cancer cell proliferation and induce apoptosis. *Lactobacillus* rhamnosus GG, for example, produces short-chain fatty acids that induce apoptosis in colorectal cancer cells by reducing matrix metalloproteinase-9 levels and increasing tight junction protein zona occludens-1 and

S. Yi, E. Jung, H. Kim, J. Choi, S. Kim, E.-K. Lim, T. Kang, J. Jung
Bionanotechnology Research Center
Korea Research Institute of Bioscience and Biotechnology (KRIBB)
125 Gwahak-ro, Yuseong-gu, Daejeon 34141, Republic of Korea
E-mail: kangtaejoon@kribb.re.kr; jjung@kribb.re.kr
J. Choi
College of Pharmacy
Korea University
Sejong 30019, Republic of Korea

The ORCID identification number(s) for the author(s) of this article can be found under https://doi.org/10.1002/smll.202406094

DOI: 10.1002/smll.202406094

S. Kim
Department of Fundamental Pharmaceutical Sciences
Graduate School
Kyung Hee University
26 Kyungheedae-Ro, Dongdaemun-Gu, Seoul 02447, Republic of Korea
E.-K. Lim, J. Jung
Department of Nanobiotechnology
KRIBB School of Biotechnology
UST
217 Gajeong-ro, Yuseong-gu, Daejeon 34113, Republic of Korea
E.-K. Lim, T. Kang, J. Jung
School of Pharmacy
Sungkyunkwan University
2066 Seobu-ro, Jangan-gu, Suwon 16419, Republic of Korea
K.-S. Kim
Department of Chemistry and Chemistry Institute for Functional Materials
Pusan National University
2 Busandaehak-ro, Geumjeon-gu, Busan 46241, Republic of Korea

tissue inhibitor of metalloproteinase.[7] Moreover, certain probiotic strains can enhance the efficacy of chemotherapy and immunotherapy by modulating the tumor microenvironment and improving immune cell infiltration into tumors.[8] For example, Bifidobacterium breve has been shown to enhance the effectiveness of immune checkpoint inhibitors by promoting T-cell infiltration in melanoma models.[9] Probiotic-derived EVs offer several advantages over traditional cell-derived EVs: 1) They are easy and cost-effective to harvest, purify, and scale, making them practical for clinical applications.[10] 2) Since they are derived from microorganisms, they are less likely to carry harmful carcinogens or immunosuppressive substances, a concern associated with mammalian cell-derived EVs.[11] 3) These EVs are naturally adapted to survive in harsh gastrointestinal environments, making them ideal candidates for oral administration, a less-invasive route that improves patient compliance and quality of life.[12]

Lactobacillus reuteri (*L. reuteri*) is a Gram-positive probiotic bacterium naturally found in the human gut. It is widely used as a supplement for promoting gastrointestinal health due to its high survival rate in the gastrointestinal tract.[13] *L. reuteri*-derived EVs (REVs) have been reported to enhance intestinal immunity and repair lipopolysaccharide-induced intestinal injury. However, the therapeutic efficacy of REVs in cancer treatment remains unexplored.[14] In this study, we report, for the first time, the therapeutic efficacy of orally administered REVs in cancer treatment. First, we confirmed the therapeutic effects of REVs through the modulation of apoptotic signaling pathways in A549 cells and a murine model. We then demonstrated that REVs in combination with other drugs, achieved potent tumor ablation and immunogenic cell death. REVs encapsulating indocyanine green (REV-ICG) were found to completely eliminate tumors within 32 d of photothermal therapy (PTT). We explored the anti-tumor mechanisms of REVs and REV-ICG using various assays. Combining REV-ICG with near-infrared (NIR) irradiation not only reduced cell proliferation and angiogenesis, as confirmed by Ki67 and CD31 staining but also enhanced calreticulin (CRT) exposure, signifying a strong induction of immunogenic cancer cell death (ICD). This combination therapy has the potential to inhibit tumor growth and boost the anti-tumor immune response. REVs can be used independently or in combination with other treatments and hold significant promise as biomaterials for cancer treatment. We anticipate that these findings will lead to the development of novel cancer treatment modalities that leverage the properties of probiotic-derived EVs.

2. Results

2.1. Preparation and Characterization of REVs

To obtain REVs, *L. reuteri* culture medium was filtered, ultracentrifuged, washed, and dispersed in phosphate-buffered saline (PBS) (**Figure** 1a). The yield was ≈20 mg L^{-1} of protein, with a particle concentration of 1.2×10^9 particles mL^{-1}, corresponding to a particle-to-protein ratio of ≈6.3×10^{10} particles mg^{-1}. The purified REVs exhibited a spherical shape with an average size of 35 ± 0.54 nm, a polydispersity index (PDI) of 0.38 ± 0.01, and a surface charge of −18 ± 0.92 mV (Figure 1b,c). Stability testing revealed that the REVs exhibited minimal changes in size when exposed pH 1, 2, and 7 solutions over 24 h (Figure 1d), indicating their robust stability.

2.2. In Vitro Cytotoxicity of REVs

REVs were selected based on preliminary cell counting kit-8 (CCK-8) assay results, which demonstrated superior therapeutic efficacy compared to other probiotic sources, including *Lacticaseibacillus paracasei*, *Lactobacillus pentosus*, and *Lactiplantibacillus plantarum* (Figure S1, Supporting Information). While REVs have been reported for USD in inflammatory diseases,[13] their effects on cancer had not been previously investigated. Therefore, we evaluated the intrinsic therapeutic efficacy of REVs cancer. First, we confirmed the cellular internalization of REV-FITC in A549 cells. After incubation, the cells were stained with 4′,6-diamidino-2-phenylindole (DAPI), and CellMask to visualize nuclei and cell membranes. Fluorescence images showed green fluorescence confined to the cytoplasm (**Figure** 2a), confirming effective cellular uptake of the REVs. Next, we performed a CCK-8 assay to determine the cytotoxicity of REVs. The results (Figure 2b) showed that REVs killed 30%, 50%, and 70% of A549 cells at concentrations of 10, 20, and 30 μg mL^{-1}, respectively, consistent with an IC_{50} value of 21.31 ± 0.5 μg mL^{-1} (Figure S2a, Supporting Information). Notably, REVs were toxic to a variety of lung cancer cell lines, including H460, PC-9, H1299, H441, HCC827, and H520 (Figure S2b, Supporting Information). Furthermore, REVs exhibited cytotoxicity against other cancer cell lines, such as A431, MM231, T47D, BT474, MCF7, and PC3 (Figure S2c, Supporting Information). In contrast, REVs showed no toxicity toward BEAS-2B (epithelial), RAW264.7 (macrophage), and NIH3T3 (fibroblast), demonstrating the selective killing effect of REVs on cancer cells (Figure S2d, Supporting Information). Flow cytometry using Annexin V-FITC/propidium iodide (PI) further confirmed that REV-induced cell death in A549 cells increased with increasing REV concentrations (Figure 2c). Moreover, PI staining for cell cycle distribution showed that the proportion of cells in the G0/G1 phase increased, whereas those in the S and G2/M phases decreased with increasing REV concentration. This suggests that REVs interfere with A549 cell growth through G2/M phase cell cycle arrest (Figure 2d). To further understand the mechanisms of REV-induced cell death, we analyzed the expression of apoptosis-related proteins, such as B-cell lymphoma-2 (Bcl-2), Bcl-2-associated X (Bax), caspase-3, cleaved caspase-3, poly (ADP-ribose) polymerase (PARP), and cleaved PARP (Figure 2e). The results showed exclusive cleavage of caspase-3 and PARP in REV-treated cells, along with a notable reduction in their expression levels. Additionally, the expression of the anti-apoptotic protein Bcl-2 was significantly reduced, whereas that of the pro-apoptotic protein Bax was upregulated, suggesting that REVs induce apoptosis by shifting the balance toward pro-apoptotic signaling. In addition to analyzing apoptosis-related proteins, the mRNA expression levels of caspase-9, Apoptotic protease activating factor-1 (APAF), Bcl-2, and Bax were measured (Figure S3, Supporting Information). REV treatment significantly increased the mRNA level of caspase-9 and APAF, indicating the upregulation of intrinsic apoptotic pathways. Furthermore, Bax mRNA was

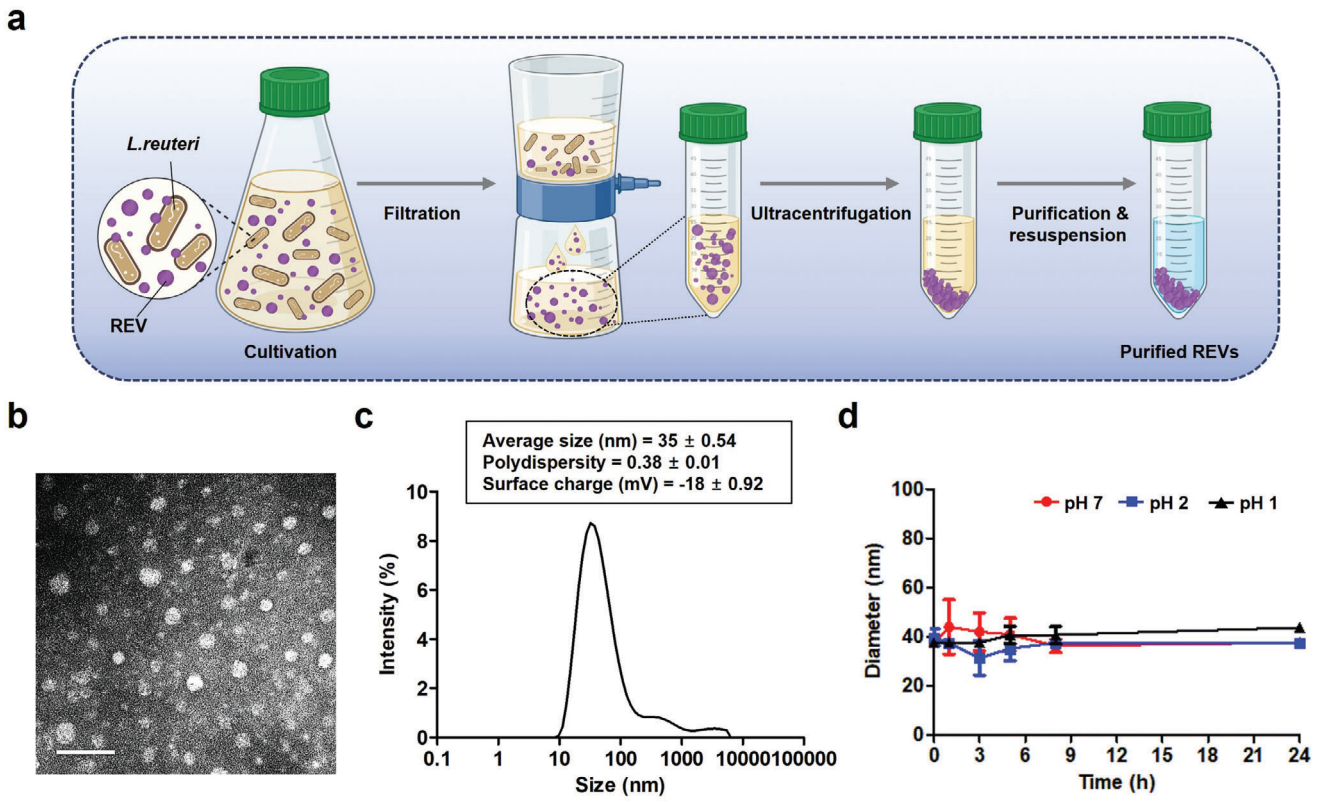

Figure 1. Preparation and Characterization of REVs. a) Schematic illustration depicting the isolation and purification process of REVs. b) Transmission electron microscopy (TEM) image displaying the morphology of REVs, with a scale bar representing 100 nm. c) Graph showing the size distribution of REVs, with an inset box detailing the average diameter, polydispersity index, and surface charge. d) Stability assessment of REVs across different pH values. Data are presented as mean ± standard deviation ($n = 3$).

upregulated, and Bcl-2 mRNA was downregulated, consistent with the protein data (Figure 2e). These finding suggest that REVs induce apoptosis by promoting pro-apoptotic gene expression while simultaneously inhibiting anti-apoptotic signals. We also investigated the effect of REVs on mitogen-activated protein kinase (MAPK) and nuclear factor kappa B (NF-κB) signaling pathways, which play important roles in tumor cell proliferation, survival, and invasion. REV treatment inhibited p65 protein expression and reduced the phosphorylation of p38, p44/42, p65, and AKT1 (Figure S4, Supporting Information), suggesting that REVs can regulate these signaling pathways to inhibit cancer cell proliferation and survival. Additionally, REVs also exhibited significant anti-inflammatory effects by regulating anti-inflammatory cytokines (interleukin (IL)-10 and transforming growth factor (TGF)-β), pro-inflammatory cytokines (tumor necrosis factor-α (TNF-α), IL-1β, IL-6, IL-17, and inducible nitric oxide synthase (iNOS)), as well as nitric oxide (NO) production (Figure S5a, Supporting Information). Flow cytometry analysis of NO levels (Figure S5b, Supporting Information) excluded debris and unstained cells, ensuring accurate measurement. These findings indicate that REVs exhibit anticancer properties by modulating cell signaling pathways, suggesting their potential as a standalone in cancer therapy. Understanding REV-induced cancer cell death pathways provides critical insights into the survival mechanisms of cancer cells and may enable the development of more sophisticated therapeutic strategies.

Additionally, the effects of REVs on cell migration were evaluated. The invasion assay demonstrated that REV concentrations of 10, 20, and 30 μg mL^{-1} reduced cell invasion by 12 ± 0.7, 87 ± 5.7, and 99% ± 0.8%, respectively (Figure 2f; Figure S6a, Supporting Information). The transwell mitigation assay showed that cell migration decreased by 65 ± 2.1, 74.6 ± 1.5, and 92.5% ± 0.7% at REV concentrations of 10, 20, and 30 μg mL^{-1}, respectively (Figure 2g; Figure S6b, Supporting Information). Finally, wound closure rates were 71.5 ± 9.7, 48.3 ± 9.5, and 39% ± 5.8% at REV concentrations of 10, 20, and 30 μg mL^{-1}, respectively (Figure 2h; Figure S6c, Supporting Information). These results indicate that REVs not only inhibit tumor cell growth but also regulate metastasis-related properties, including cell invasion and migration.

2.3. In Vivo Antitumor Activity of REVs

The anti-tumor activity of REVs was investigated in a murine model of A549 tumors. REVs were administered orally to the murine model at specified time points (**Figure 3a**), and tumor size was monitored. As shown in Figure 3b,c, REVs significantly inhibited tumor growth. After 32 days, tumor volume and tumor weight were reduced by ≈435 ± 67 mm^3 and 407 ± 38 mg, respectively, in mice orally treated with REVs compared to those treated with PBS (the control). However, the weights of the mice

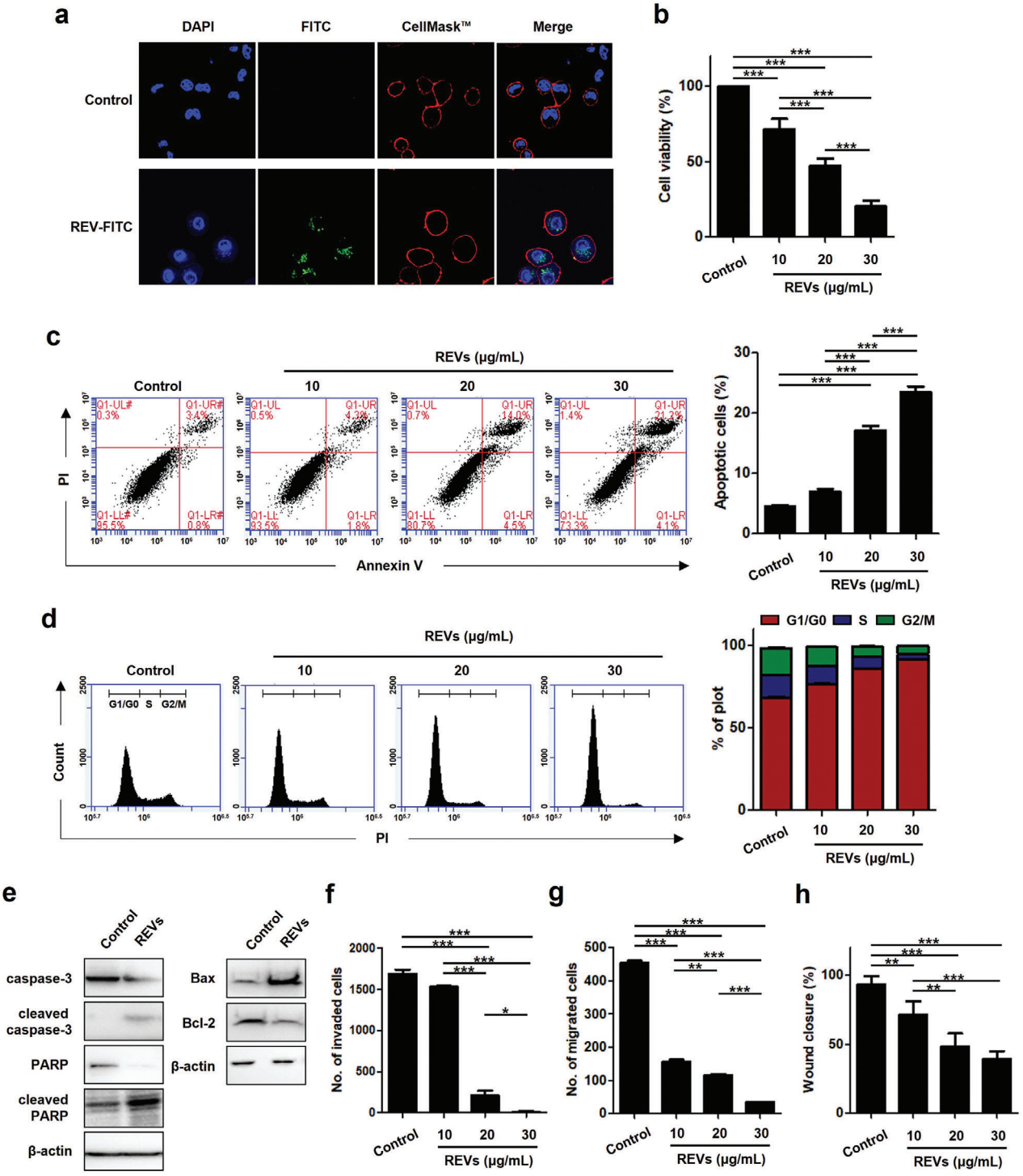

Figure 2. In Vitro Cytotoxicity of REVs. a) Visualization of cellular uptake of REVs, confirming internalization. b) Dose-dependent cytotoxicity of REVs showing significant cell death. Data are presented as mean ± standard deviation ($n = 5$) and statistical significance is assessed using one-way ANOVA with a *post hoc* Tukey's HSD test (***$p < 0.001$). c) Flow cytometry analysis illustrating increased apoptosis induced by REVs. Data are presented as mean ± standard deviation ($n = 5$) and statistical significance (***$p < 0.001$). d) Analysis of cell cycle arrest effects of REVs, indicating phase-specific impacts. Data are presented as mean ± standard deviation ($n = 5$). e) Western blot analysis depicting the activation of apoptosis-related proteins by REVs in A549 cells. f) Invasion assay demonstrating the inhibitory effect of REVs on cancer cell invasiveness. Data are presented as mean ± standard deviation ($n = 5$) and statistical significance (*$p < 0.05$ and ***$p < 0.001$). g) Transwell migration assay highlighting reduced cell migration due to REV treatment. Data are presented as mean ± standard deviation ($n = 5$) and statistical significance (**$p < 0.01$ and ***$p < 0.001$). h) Wound closure assay showing decreased migration rates in REV-treated cells. Data are presented as mean ± standard deviation ($n = 5$) and statistical significance (**$p < 0.01$ and ***$p < 0.001$).

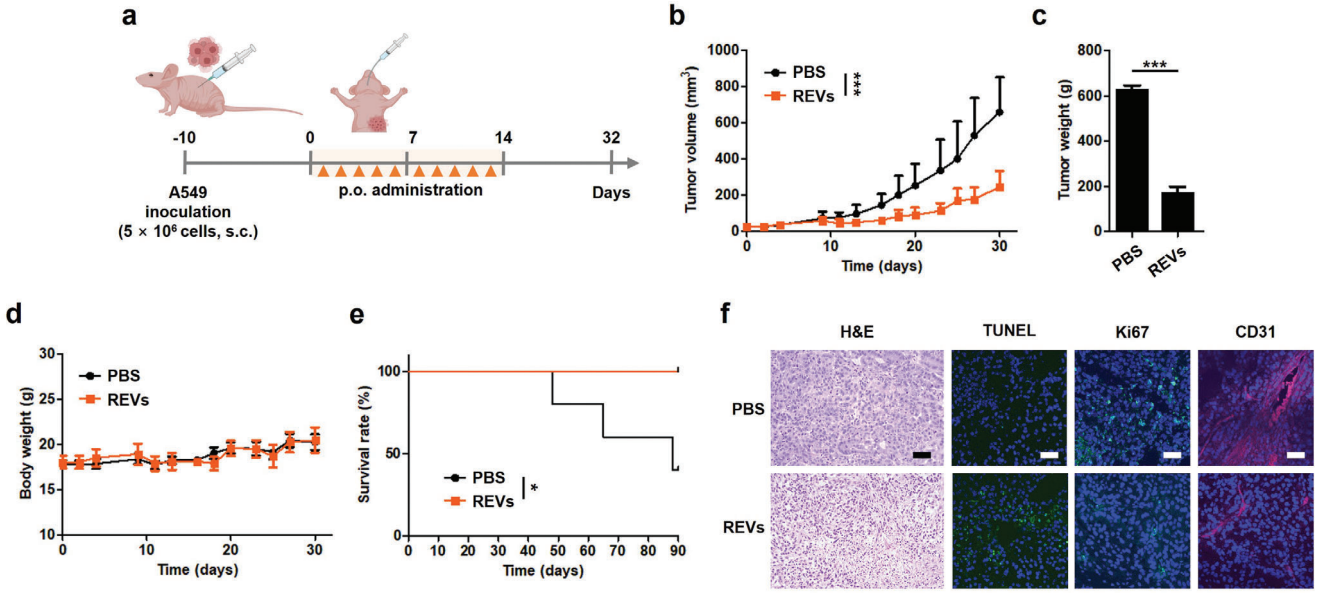

Figure 3. In Vivo Antitumor Activity of REVs. a) Timeline of the experimental treatment protocol with REVs. b) Tumor growth curves illustrating the effect of REVs on tumor progression in mice, with each point representing the average tumor volume over time. Data are presented as mean ± standard deviation ($n = 5$) and statistical significance is assessed using Student's t-test (***$p < 0.001$). c) Weights of tumors excised from mice on day 32, showing the efficacy of REVs in tumor reduction. Data are presented as mean ± standard deviation ($n = 5$) and statistical significance (***$p < 0.001$). d) Body weight of mice during the treatment period. Data are presented as mean ± standard deviation ($n = 5$) and statistical significance is assessed using Student's t-test (***$p < 0.001$). e) Mice survival over 90 d. Data are presented as mean ± standard deviation ($n = 5$) and statistical significance is assessed using the log-rank (Mantel-Cox) test (*$p < 0.05$). f) Histological analysis of tumors treated with REVs, harvested on day 32 and stained with H&E and TUNEL for apoptosis, and Ki67 and CD31 for cell proliferation and angiogenesis. Scale bars represent 200 µm for H&E and 50 µm for fluorescence images.

remained virtually unchanged over the 32-day period, regardless of treatment (Figure 3d). The survival of tumor-bearing mice was monitored for 90 days. In the REV-treated group, all mice survived throughout the 90-day period, whereas several deaths occurred in the PBS-treated control group. (Figure 3e). Examination of harvested tumors using H&E staining and terminal deoxynucleotidyl transferase dUTP nick end labeling (TUNEL) staining indicated that cell death was enhanced in REV-treated tumors compared to PBS-treated tumors, indicating that REVs directly induce tumor cell death (Figure 3f). Further staining of tumor tissues for Ki67 and CD31 revealed decreased expression of both markers in REV-treated tumors, indicating inhibition of cell proliferation and angiogenesis (Figure 3f). Since angiogenesis is essential for tumor growth and metastasis, these results suggest that REVs may inhibit angiogenesis as part of their anticancer mechanism, providing an important strategy to prevent tumor spread and enhance treatment efficacy. Collectively, these results highlight the potential of REVs as cancer therapeutic agents, given their ability to affect a range of biological pathways involved in tumor growth and metastasis.

2.4. Preparation and Characterization of REV-ICG

The results of both cell and animal experiments demonstrated that REVs exert cancer therapeutic effects when administered independently. Interestingly, REVs can also serve as drug delivery platforms in addition to their role as cancer therapeutic agents, offering higher safety and encapsulation efficiency compared to conventional synthetic nanocarriers. To develop a combination treatment strategy, ICG, a Food and Drug Administration-approved sensitizer for PTT and clinical imaging was loaded onto REVs, with the objective of maximizing the effectiveness of cancer therapy.[15] However, its independent use is limited by its low aqueous stability, rapid elimination under physiological conditions, and susceptibility to thermal and photodegradation, especially in acidic environments.[16] We anticipated that REV-ICG would provide efficient and stable cancer therapy due to the synergistic effect of the two materials.

REV-ICG was easily prepared by incubation (**Figure** 4a). After 4 h of incubation at 37 °C, the purified REV-ICG retained a uniform spherical shape, with a diameter of 38.38 ± 9.18 nm and a PDI of 0.54 ± 0.19, similar to native REVs (Figure 4b,c). The surface charge of REV-ICG also remained almost unchanged at −17.5 ± 0.56 mV, comparable to that of REVs. Ultraviolet-visible (UV–Vis) measurements demonstrated that REV-ICG had a slightly broadened and red-shifted absorption peak (800 nm) compared to free ICG (780 nm), likely due to interactions between ICG and REVs (Figure 4d). Fluorescence measurements showed that 0.53 mg mL^{-1} of ICG was encapsulated in 1 mg mL^{-1} REV, resulting in a loading efficiency (LE) of 79.4 ± 8% and a loading capacity (LC) of 52.4 ± 5% (Figure S7, Supporting Information).

To investigate the photothermal performance of REV-ICG, a sample was irradiated with a NIR laser at a power density of 1 W cm^{-2}. A temperature change of 38 °C (Δ 38 °C) was observed for REV-ICG, comparable to the 43 °C (Δ 43 °C) observed for free ICG, whereas REV alone demonstrated a negligible

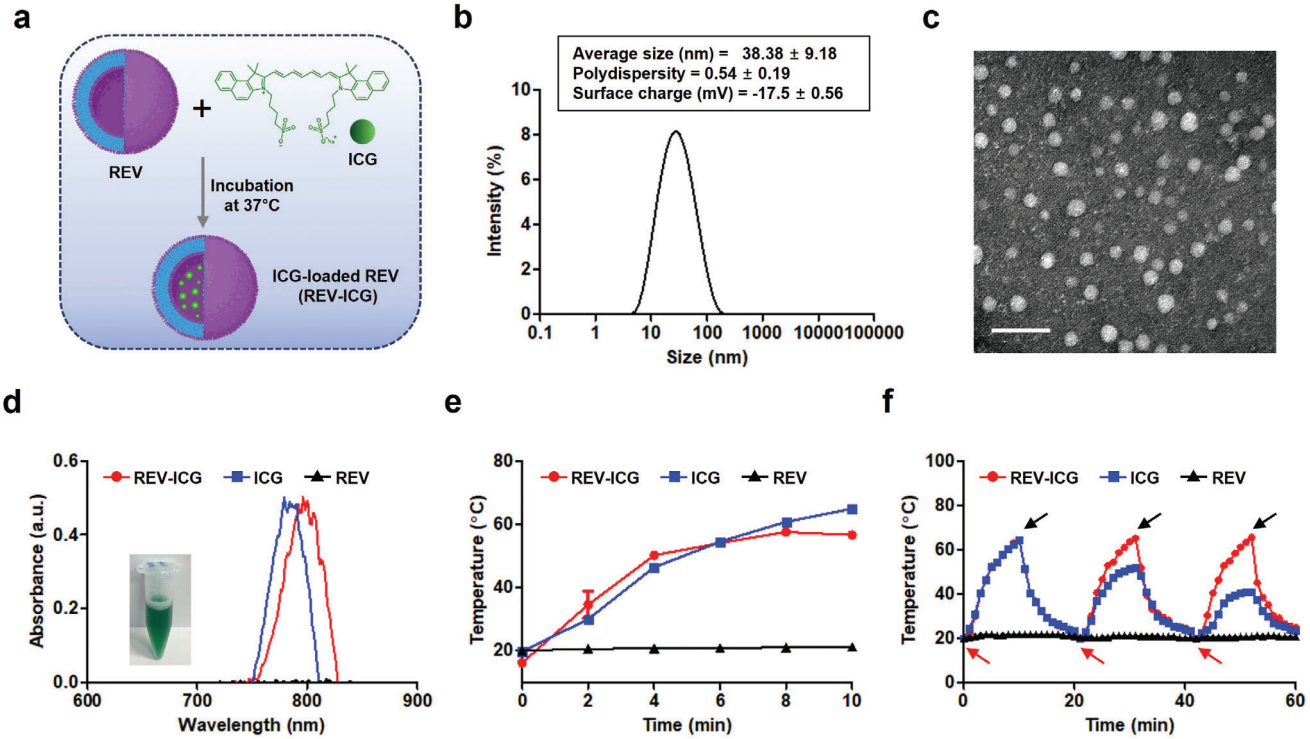

Figure 4. Preparation and Characterization of REV-ICG. a) Schematic illustration showing the preparation process of REV-ICG. b) Graph showing the size distribution of REV-ICG, with an inset box detailing the average diameter, polydispersity index, and surface charge. c) TEM image displaying the morphology of REV-ICG, with a scale bar representing 100 nm. d) UV–Vis absorbance spectra comparing REV-ICG, free ICG, and REV. The inset shows REV-ICG dispersed in PBS. e) Temperature change profiles under a NIR laser irradiation (1 W cm^{-2}) over 10 min. Data are presented as mean ± standard deviation ($n = 3$). f) Temperature changes of REV-ICG, free ICG, and REV during three cycles of laser on/off (1 W cm^{-2}), with red arrows indicating laser on and black arrows indicating laser off.

temperature change (Δ 5 °C) (Figure 4e; Figure S8a, Supporting Information). Notably, REV-ICG showed a consistent temperature increase compared to ICG under repeated laser irradiation (Figure 4f). Moreover, REV-ICG demonstrated greater temperature changes across various concentrations and laser intensities (Figure S8b,c, Supporting Information). These findings indicated the remarkable photothermal efficacy of REV-ICG, suggesting its potential as an effective PTT material.

2.5. Enhanced Cytotoxicity of REV-ICG

To confirm the phototherapeutic efficacy of REV-ICG, we evaluated its cytotoxicity (**Figure** 5a). A concentration of 20 μg mL^{-1} REV-ICG was selected based on IC_{50} data and experimental observations (Figure 2b; Figure S2a, Supporting Information), where REV alone achieved a 50% cell suppression rate at this concentration. This concentration was considered optimal as it balanced therapeutic efficacy with experimental feasibility for further studies. In the absence of NIR irradiation, 20 μg mL^{-1} REV-ICG resulted in 50% cell viability, comparable to REV alone (Figure 2b). However, following NIR irradiation, REV-ICG significantly enhanced cell death, reducing cell viability by an additional 16%. In contrast, free ICG exhibited 97% cell viability, regardless of laser irradiation, whereas REV-ICG exhibited a notable increase in its capacity to induce cancer cell deaths. Furthermore, calcein-AM and PI staining of A549 cells demonstrated predominant red fluorescence after REV-ICG treatment and NIR irradiation, indicating that the synergistic effect of REVs and PTT led to enhanced cytotoxicity (Figure 5b).

Reactive oxygen species (ROS) are important mediators of various cellular processes, including cell proliferation, differentiation, migration, and death.[17] To investigate the relationship between ROS production and apoptosis after PTT with REV-ICG, we used the CellRox Green marker to confirm ROS generation (Figure 5c; Figure S9a, Supporting Information). The results demonstrated a significant increase in ROS levels when cells were treated with REV-ICG and irradiated with NIR light. To quantify cell death due to increased ROS levels, Annexin V-FITC and PI staining were performed to identify apoptotic cells (Figure 5d; Figure S9b, Supporting Information). The results showed that cells treated with REV-ICG and subjected to NIR irradiation exhibited a significantly increased apoptosis rate of 69%, confirming the potent anticancer effects of REV-ICG combined with PTT.

2.6. Tumor Targeting and Photothermal Activities of REV-ICG

The tumor-targeting and photothermal properties of REV-ICG were evaluated in an A549 lung cancer mouse model using different administration routes, including oral (p.o.),

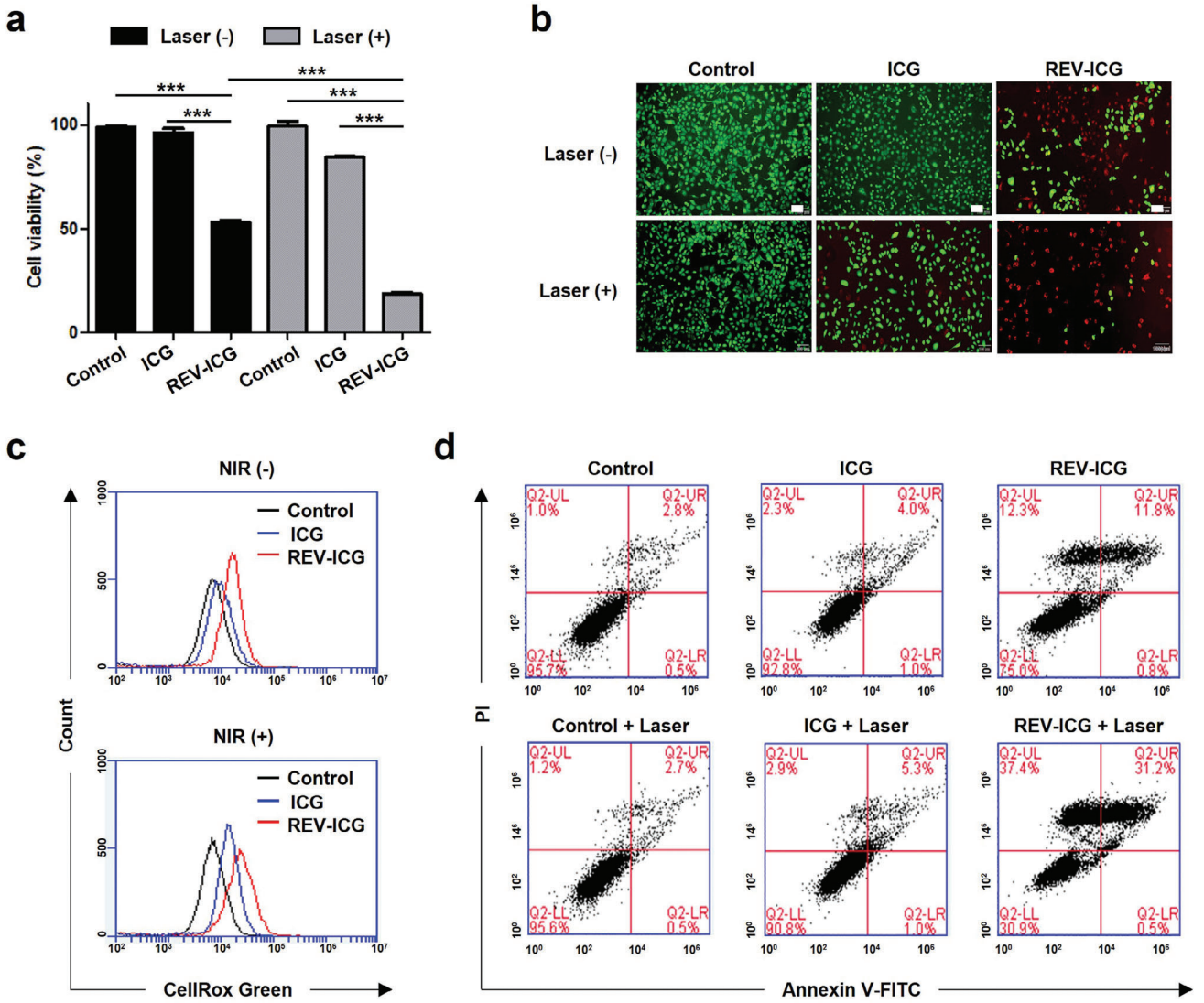

Figure 5. Enhanced Cytotoxicity of REV-ICG. a) Cytotoxicity of ICG and REV-ICG (20 μg mL^{-1}) before and after NIR laser irradiation (1 W cm^{-2}) for 5 min. Data are presented as mean ± standard deviation ($n = 5$) and statistical significance is assessed using one-way ANOVA with a *post hoc* Tukey's HSD test (***$p < 0.001$). b) Live and dead cell staining results of ICG and REV-ICG (20 μg mL^{-1}) treatment before and after NIR laser irradiation (1 W cm^{-2}) for 5 min. Scale bars represent 100 μm. c) Detection of reactive oxygen species (ROS) generation in treated cells, illustrating increased ROS production under an NIR irradiation. d) Analysis of cellular apoptosis via Annexin V-FITC and PI staining, illustrating increased apoptotic activity following REV-ICG treatment and NIR exposure.

intraperitoneal (i.p.), and intravenous (i.v.) administration. In vivo, fluorescence images conducted 24 h after drug administration revealed that REV-ICG exhibited superior tumor-targeting capability compared to free ICG (**Figure 6**a). Fluorescence images of harvested tumors further validated the tumor-targeting ability of REV-ICG (Figure 6b). This improved targeting is attributed to the ability of REVs to efficiently accumulate at tumor sites due to their enhanced permeability and retention effects, which prolonge signal retention and prevent rapid systemic clearance. Importantly, the histological evaluation showed no significant differences in efficacy among the three administration routes (p.o., i.p., and i.v.) with REV-ICG, demonstrating consistent therapeutic outcomes regardless of the route. Pharmacokinetic analysis revealed that plasma concentrations of REV-ICG varied based on the administration route. Peak concentrations occurred at 1 h (i.v.), 3 h (i.p.), and 5 h (p.o.) following administration, followed by decline due to distribution and metabolism. The area under the plasma concentration-time curve (AUC) values were 934.4 μg h mL^{-1} (p.o.), 1101 μg h mL^{-1} (i.p.), and 1414 μg h mL^{-1} (i.v.) (Figure 6c). To further assess photothermal effects, the tumor temperatures were monitored following REV-ICG administration and NIR laser irradiation (Figure 6d,e). After 5 min of laser irradiation, tumor temperature increased to 42.3 °C (p.o.), 47.1 °C (i.p.), and 48.3 °C (i.v.). In contrast, temperatures in control groups treated with PBS and free ICG increased by 3.4 °C and 6.3 °C, respectively. Free ICG was rapidly cleared from the bloodstream because of its circulating half-life of less than 5 min, resulting in poor tumor uptake and reduced

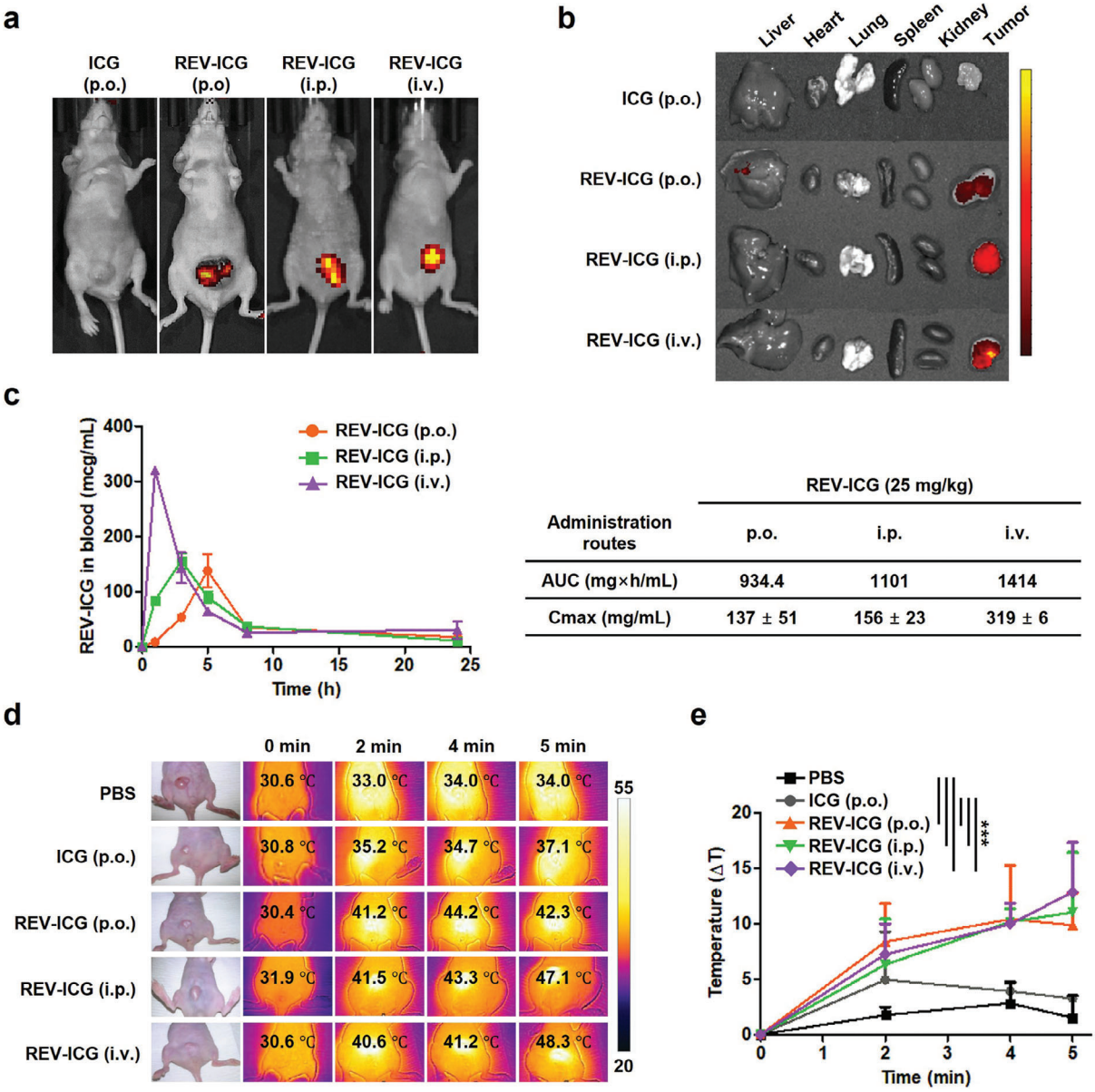

Administration routes	REV-ICG (25 mg/kg) p.o.	i.p.	i.v.
AUC (mg×h/mL)	934.4	1101	1414
Cmax (mg/mL)	137 ± 51	156 ± 23	319 ± 6

Figure 6. Tumor Targeting and Photothermal Activities of REV-ICG. a) In vivo fluorescence imaging showing the distribution of free ICG and REV-ICG (equivalent to 5 mg kg^{-1}) in mice after p.o., i.p., and i.v. administrations. b) *Ex vivo* biodistribution of free ICG and REV-ICG in harvested tissues 1 day post-administration, illustrating enhanced targeting by REV-ICG. c) Plasma concentration-time curves and pharmacokinetic parameters following p.o., i.p., and i.v. Administrations of REV-ICG. Data are presented as mean ± standard deviation ($n = 5$). d) Thermal images of A549-bearing mice during NIR laser irradiation (1 W cm^{-2}), demonstrating the photothermal response. e) Temperature change profiles of tumors over 5 min under a NIR irradiation. Data are presented as mean ± standard deviation ($n = 5$) and statistical significance (***$p < 0.001$).

photothermal effect.[18] REV-ICG effectively accumulated at tumor sites and generated significant temperature increases, demonstrating its potential for photothermal cancer therapy.

2.7. Enhanced Antitumor Activity of REV-ICG

The synergistic effect of REV-ICG and PTT was evaluated in an A549 tumor mouse model. To assess the efficacy of different administration routes and the effect of NIR laser irradiation, mice with tumor sizes of ≈30 mm^3 were divided into several groups based on treatment type (**Figure 7a**; Figure S10a, Supporting Information). These included a control group treated with PBS, groups treated with REV-ICG (via p.o., i.p., i.v.) without NIR laser irradiation, groups receiving REV-ICG via the same routes but in combination with NIR laser irradiation, and a group treated with oral ICG and NIR laser treatment. As illustrated in Figure S10b (Supporting Information), REV-ICG administration without NIR irradiation led to tumor size reductions of 68%, 80%, and 71% for p.o, i.p., and i.v., respectively, compared to

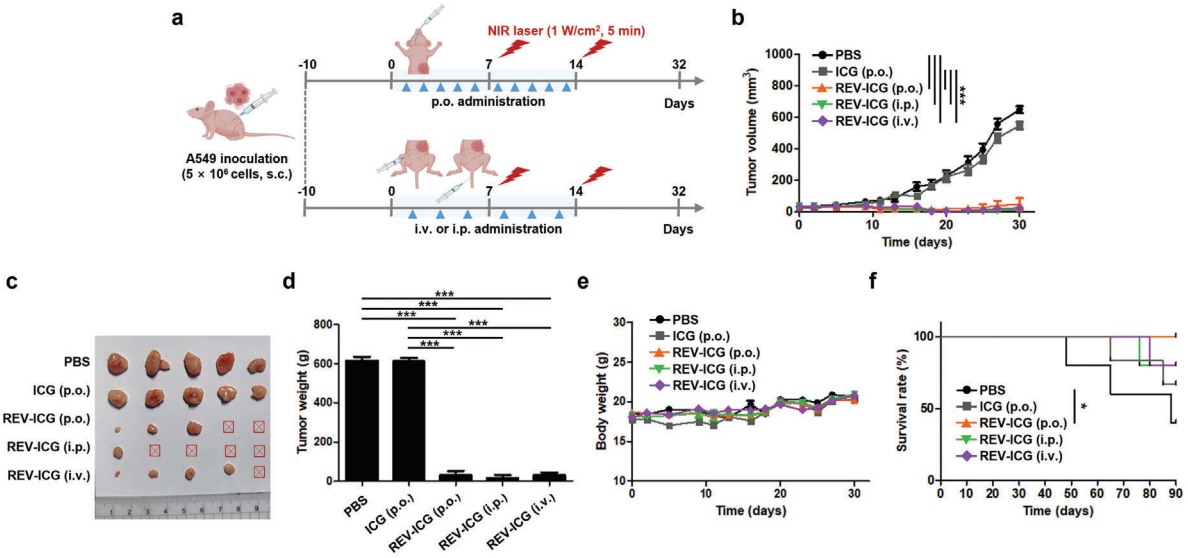

Figure 7. Anti-Tumor Activity of REV-ICG Combined with PTT. a) Timelines of experimental treatment and NIR irradiation (1 W cm^{-2}, 5 min). b) Tumor growth curves of mice from different treatment routes, highlighting the therapeutic efficacy of REV-ICG. Data are presented as mean ± standard deviation ($n = 5$) and statistical significance is assessed using one-way ANOVA with a *post hoc* Tukey's HSD test (***$p < 0.001$). c) Photographs of tumors dissected from mice on day 32, with the red crossed box indicating an invisible tumor. d) Weights of tumors excised from mice on day 32, showing a significant reduction in tumor mass. Data are presented as mean ± standard deviation ($n = 5$) and statistical significance (***$p < 0.001$). e) Body weight of mice during the treatment period. Data are presented as mean ± standard deviation ($n = 5$) and statistical significance (***$p < 0.001$). f) Mice survival over 90 d. Data are presented as mean ± standard deviation ($n = 5$) and statistical significance is assessed using the log-rank (Mantel-Cox) test (*$p < 0.05$).

the control group. Additionally, the tumors harvested 32 days after treatment displayed significantly lower weights than those in the control group (Figure S10c,d, Supporting Information). These results were comparable with those obtained with REV alone (Figure 3b,c), indicating a distinctive therapeutic effect of REVs that persisted across different administration routes. Next, we administered REV-ICG followed by NIR irradiation at the tumor sites for 5 min at a power density of 1 W cm^{-2} on days 7 and 14 (Figure 7a). As illustrated in Figure 7b, the group treated with REV-ICG and the NIR laser exhibited a pronounced decrease in therapeutic efficacy across all dosing modalities. Tumor volumes decreased by ≈217 ± 32 mm^3 (p.o.), 146 ± 27 mm^3 (i.p.), and 219 ± 36 mm^3 (i.v.) in NIR laser-irradiated tumors compared to non-irradiated ones. On day 32, tumors were excised and weighed, revealing nearly complete tumor elimination across all dosing modalities, with reductions in tumor weight of ≈119 ± 39 mg (p.o.), 106 ± 10 mg (i.p.), and 117 ± 30 mg (i.v.) in NIR laser-irradiated tumors compared to non-irradiated ones (Figure 7c,d). Notably, no significant weight loss was observed in any treatment groups over the 32-day period (Figure 7e; Figure S10e, Supporting Information). Additionally, REV-ICG, with or without PTT, significantly extended survival in mice compared to the PBS control group (Figure 7f; Figure S10f, Supporting Information). These findings suggest that the combination of REV-ICG and PTT may serve as a highly effective and well-tolerated cancer treatment strategy.

2.8. Antitumor Mechanism of REV-ICG

To investigate the anti-tumor mechanism of REV-ICG, a comprehensive histological analysis was conducted. Tumors harvested 32 days post-treatment were subjected to H&E and TUNEL staining to assess cell morphology and apoptosis, respectively (**Figure 8**; Figure S11, Supporting Information). The results showed that REV-ICG alone effectively induced cell death across all dosing regimens, with the highest cell death observed in tumors treated with REV-ICG combined with NIR irradiation. Further analysis using Ki67 and CD31 staububg revealed a significant reduction in cell proliferation and angiogenesis in the group treated with both REV-ICG and NIR irradiation (Figure 8; Figure S11, Supporting Information). This indicates a synergistic effect of REV-ICG and PTT, enhancing the anticancer effect. To further investigate the induction of ICD, histological staining was performed for high-mobility group box 1 (HMGB1) and calreticulin (CRT), two critical markers of ICD. HMGB1 is released from the nuclei of dying tumor cells into the extracellular space, signaling the immune system to recognize the tumor. CRT exposure on the cell surface further promotes immune activation. In the combination treatment group, both HMGB1 release and CRT exposure were significantly elevated compared to REV-ICG alone or the PBS control group, indicating a stronger ICD response.[19] These findings suggest that the combination of REV-ICG and NIR irradiation not only directly induces tumor cell death but also enhances the immune response by inducing ICD. This dual mechanism of action may contribute to more effective tumor elimination through direct cytotoxic effects and immune-mediated pathways.

Finally, the potential toxicity of the treatment was evaluated through histological examination of various organs and measurements of serum levels for liver and kidney function markers, including alanine aminotransferase (ALT), aspartate transaminase (AST), albumin (ALB), and creatinine (CRE). As shown in **Figure 9** and Figure S12 (Supporting Information), no

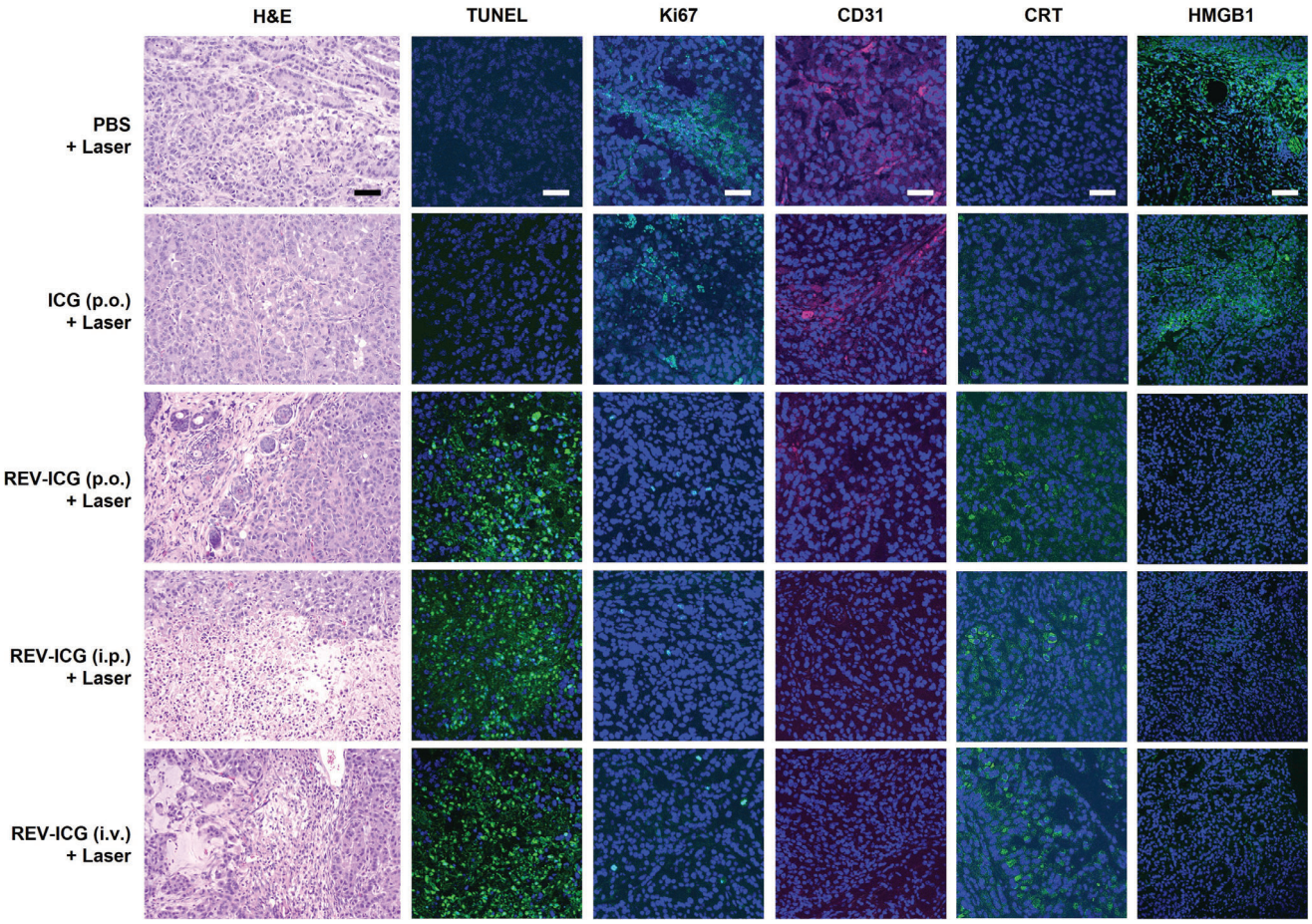

Figure 8. Histological Evaluation of Tumors Treated with REV-ICG and PTT. Tumors were harvested on day 32 and subjected to various stains to assess cellular and structural changes. H&E staining was used for general tissue architecture, while TUNEL, Ki67, CD31, CRT, and HMGB1 staining were employed to evaluate apoptosis, proliferation, angiogenesis, and immunogenic cell death, respectively. Scale bars represent 200 μm for H&E and 50 μm for fluorescence images.

significant adverse events or side effects were observed compared to the PBS control group, confirming the safety of REVs as therapeutic agents and drug delivery platforms. These results demonstrate that REV-ICG has the potential to be an effective and safe anti-cancer therapy. Additionally, this study provides an important foundation for exploring the potential of REV-ICG in tumor treatment and its application in various disease states.

3. Discussion

In recent years, EVs derived from various sources, including cancer cells,[20] immune cells,[5] plants,[21] and food[22] have been extensively studied for their potential in drug delivery and therapeutic applications in oncology and other diseases. However, several key challenges, such as ethical concerns, safety, therapeutic effectiveness, and standardization, continue to impede their clinical application. In this context, bacteria, particularly probiotics, have emerged as optimal cell sources due to their therapeutic effectiveness, safety profile, stability within the human body, and cost-effective scalability. Among these strains, L. reuteri was selected for its notable anti-inflammatory and anticancer properties, making it a promising candidate for therapeutic applications. Although the use of REVs in inflammatory diseases is well established, their application in cancer therapy remains unexplored. This study provides the first evidence of the intrinsic antitumor mechanisms of REVs. We demonstrated that REVs induce apoptosis and cell cycle arrest in A549 lung cancer cells through the MAPK pathway, which is affected by oxidative stress. Furthermore, REVs inhibited cell invasion and migration, suggesting their potential role in preventing cancer metastasis. These results highlight the potential of REVs as a natural and effective medium for cancer therapy. In addition, by encapsulating the NIR dye ICG within REVs, we addressed limitations such as heterogeneous heat distribution, light scattering, and rapid dye removal.[16] Our approach leveraged the unique properties of REVs to improve the stability and delivery efficiency of ICG, thereby enhancing the therapeutic effect of PTT in cancer treatment. The combination of REV-ICG and PTT not only significantly reduces tumor size, but also induces ICD, which releases tumor-associated antigens and stimulates immune responses, probiding additional therapeutic benefits beyond direct tumor destruction. An important finding was the flexibility of REV-ICG administration. Whether administered p.o., i.p., or i.v., REV-ICG maintained high delivery efficiency and therapeutic efficacy. This adaptability is attributed

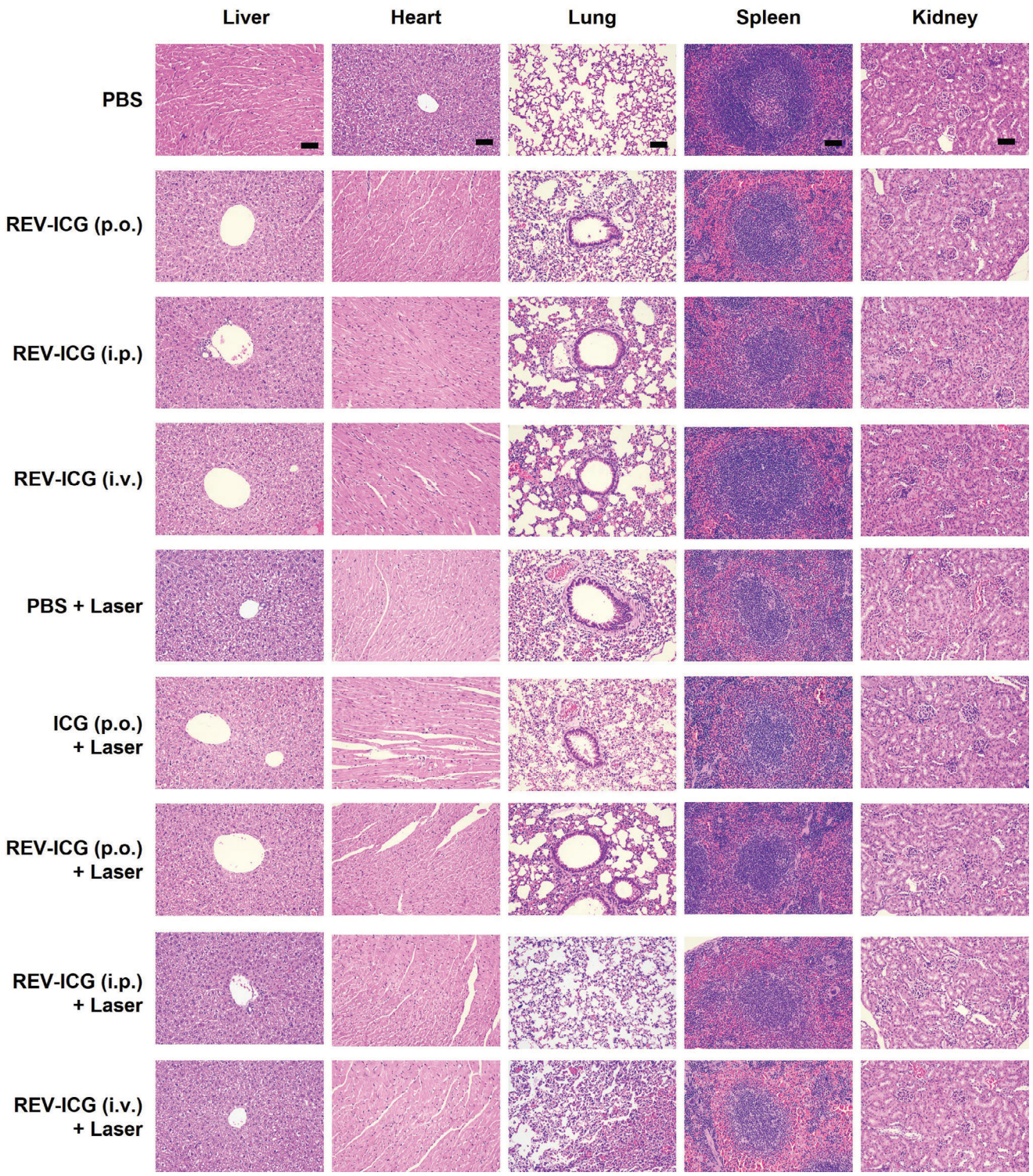

Figure 9. Biocompatibility of REV-ICG. Tumors and major organs (liver, heart, lung, spleen, and kidney) stained with H&E. Scale bars represent 200 µm.

to the robust, environmentally stable nature of REVs, which exhibit greater stability compared to other drug delivery systems such as liposomes.[23] While liposomes often face challenges, such as leakage and premature drug release, REV-ICG exhibits excellent stability, minimizing these issues and ensuring more reliable drug delivery. This robust stability allows for customized treatment strategies based on individual patient needs and preferences, making REV-ICG a versatile therapeutic option. In this study, we demonstrated the therapeutic potential of REVs, both as a monotherapy and in combination with PTT. For successful

clinical translation, we propose integrating REVs with existing treatment modalities, such as chemotherapy, radiotherapy, and immunotherapy, to enhance therapeutic outcomes. Future studies should address several critical challenges, including the complexities of scaled-up production, regulatory requirements, and ensuring rigorous safety and efficacy evaluations through comprehensive clinical trials. While the results of the 32 days toxicity study (Figure 9; Figure S12, Supporting Information) are promising, further long-term studies, including assessments of biodistribution, clearance, and potential side effects, are necessary to fully evaluate the safety profile and facilitate the transition of this therapeutic strategy from preclinical research to clinical application. These studies will also provide valuable insights into dosage optimization, contributing to the establishment of a well-defined therapeutic index.

4. Conclusion

This study demonstrates the significant potential of REVs as a novel therapeutic approach for cancer treatment. Through extensive in vitro and in vivo experiments, we have demonstrated that REVs possess intrinsic anti-tumor properties and inhibit cancer cell invasion and migration, indicating their potential role in preventing metastasis. Additionally, we investigated the potential of REVs as drug delivery platforms by encapsulating ICG to create REV-ICG. This combination significantly enhanced the PTT efficacy, reduced tumor size, and induced ICD when combined with NIR laser irradiation. The versatility and potential clinical applications of REV-ICG were confirmed by its stability and therapeutic efficacy across different administration routes (p.o., i.p., and i.v.). The findings from this study establish REVs as a promising standalone cancer therapy and as a robust drug delivery platform that can enhance existing treatments such as PTT. The inherent stability of REVs in the gastrointestinal tract and their ability for natural engineering make them a practical solution for future cancer therapies. This study paves the way for the development of advanced cancer treatments that leverage the unique benefits of probiotic-derived EVs.

5. Experimental Section

Isolation and Characterization of REVs: *L. reuteri* was cultivated at 37 °C and 150 rpm in a man-ragosa-sharpe (MRS) medium (Thermo Fisher Scientific, Waltham, MA, USA), as reported previously.[14] The culture medium was filtered through a 0.22 µm membrane filter to remove bacteria and debris, followed by ultracentrifugation at 100 000 g for 3 h at 4 °C to isolate and collect REVs. The REVs were purified through multiple washes with PBS using ultracentrifugation. Purified REVs were dispersed in PBS and stored at 4 °C until further analysis. The concentration of REVs was measured using the Bradford assay (Thermo Fisher Scientific), and particle numbers were calculated using a nanoparticle size analyzer (PMX 430, Particle Metrix, Germany). The size distribution and surface charge of the REVs, REVs were measured by diluting them to 0.1 mg mL^{-1} in PBS and analyzing them with a Zetasizer Nano ZSP/Zen5600 (Malvern Panalytical, UK). For TEM imaging, samples were loaded onto Formvar carbon film-coated with 400-mesh hexagonal copper grids (Thermo Fisher Scientific) at a concentration of 0.1 mg mL^{-1} in PBS, followed by staining with 2% uranyl acetate (Thermo Fisher Scientific). Samples were imaged at 120 kV using a Tecnai G2 Spirit Twin (FEI Company, Hillsboro, OR, USA). The stability of the REVs was assessed at different pH values (pH 1, 2, and 7) by measuring their size changes over 24 h.

Preparation and Photochemical Characterization of REV-ICG: REV-ICG was prepared by incubating REVs and ICG, as described previously.[24] In brief, REVs (15 mg mL^{-1}) and ICG (10 mg mL^{-1}) were mixed in a 1.5: 1 mass ratio and then incubated at 37 °C for 4 h. Excess ICG was removed using a dialysis membrane against PBS for 4 h. The ICG loading amount in the REVs was quantified by comparing their fluorescence (excitation/emission (nm) = 785/811) with that of free ICG using a fluorescence spectrometer (Horiba, Japan). Drug LE and LC were calculated using the following equations: LE (%) = (total amount of drug encapsulated/total amount of drug added) × 100, and LC (%) = (total amount of drug encapsulated/amount of drug-loaded REVs) × 100. The red shift of the absorbance spectra of REV-ICG and ICG (0.1 mg mL^{-1} in PBS) was measured using a UV–Vis spectrometer (NanoDrop 2000c, Thermo Fisher Scientific). The temperature changes in REV-ICG and ICG (1 mg mL^{-1} in PBS, $n = 3$) under a NIR laser (1 W cm^{-2}) was measured for 10 min at 1-min intervals using a thermal camera (FLIR, Wilsonville, OR, USA). Photostability was assessed by exposing REV-ICG and ICG (1 mg mL^{-1} in PBS) to NIR laser for 10 min, followed by a 10-min cooling period with the laser turned off. This laser on/off cycle was repeated three times, with temperatures recorded at 1-min intervals using a thermal camera.

Cellular Uptake: To investigate the cellular internalization of REVs, fluorescein isothiocyanate-loaded REV (REV-FITC) was prepared as mentioned above used for preparing REV-ICG.[24] REV and FITC were combined in a mixture at a mass ratio of 1.5: 1 and incubated at 37 °C for 4 h. The resulting mixture was then purified by dialysis. A549 cells (5×10^6 cells per well) were seeded in a glass bottom dish and treated with REV-FITC at a concentration of 10 µg mL^{-1}. After 24 h incubation, cells were washed three times with PBS and additionally stained with DAPI (Thermo Fisher Scientific) and CellMask (Thermo Fisher Scientific) to visualize nuclei and cell membrane, respectively. Fluorescence images were acquired using a confocal laser scanning microscope (CLSM, Olympus, Japan).

Cytotoxicity Evaluation: The cytotoxicity was determined by a CCK-8 assay. To evaluate dose-dependent cytotoxicity and sensitivity, A549, H460, PC-9, H1299, H441, HCC827, H520, A431, MM231, T47D, BT474, MCF7, PC3, BEAS-2B, RAW264.7, and NIH3T3 were treated with REVs at concentrations of 10, 20, and 30 µg mL^{-1} and incubated for 24 h ($n = 5$). To investigate synergistic phototherapy, A549 cells (5×10^6 cells per well) were incubated with REVs or REV-ICG (20 µg mL^{-1}, $n = 5$) for 6 h and exposed to NIR laser (1 W cm^{-2}) for 5 min followed by additional incubation for 18 h. A549 cells were incubated with CCK-8 solution for 4 h, and then the absorbance was recorded on a microplate reader (Tecan, Switzerland) at 450 nm. The cell viability (%) was determined by comparing the absorbance with those of untreated cells. To visualize cell viability, cells were stained with calcein-AM and PI solution using a live/dead staining kit (Thermo Fisher Scientific), followed by the manufacturer's instructions. The fluorescence images were acquired with CLSM.

ROS Generation, Apoptosis, and Cell Cycle Analysis: A549 cells (5×10^6 cells per well) were seeded in 24-well plates. REVs and REV-ICG (20 µg mL^{-1}, $n = 3$–5) were treated with or without NIR exposure (808 nm, 1 W cm^{-2}, 5 min). NIR laser irradiation was applied 6 h post-treatment, followed by an additional 18 h of cell incubation. To assess intracellular ROS level, cells were stained using the CellROX kit (Thermo Fisher Scientific). To quantify the rate of apoptosis, A549 cells were stained with Annexin V-FITC and PI following the manufacturer's instructions (BD Bioscience, Franklin Lakes, NJ, USA). For the analysis of the cell cycle, cells were fixed in 70% ethanol and stained with PI. Stained cells were then analyzed using flow cytometry (BD Biosciences).

Western Blotting: After treatment with REVs, cells were lysed in radioimmunoprecipitation assay buffer (Thermo Fisher Scientific) containing protease and phosphatase inhibitors. The lysates were boiled in 4× sodium dodecyl sulfate sample buffer (Thermo Fisher Scientific) for 5 min. Protein samples were separated by electrophoresis and transferred to polyvinylidene fluoride membrane (Thermo Fisher Scientific). Membranes were blocked with 5% skim milk in TBST (0.05% Tween-20 in tris phosphate-buffered saline (TBS)) for 1 h at 25 °C. The membranes were then incubated with the appropriate antibodies in 5% skim milk for 16 h at 4 °C, followed by incubation with secondary antibodies in TBST for 1 h at 25 °C. Proteins were detected using a chemiluminescence kit

(Thermo Fisher Scientific). The expression of proteins was detected using specific antibodies (Cell Signaling Technology, Danvers, MA, USA), including Bcl-2 (7382), Bax (2772), caspase-3 (14 220), cleaved caspase-3 (9664), PARP (9542), cleaved PARP (5625), p65 (8242), phosphorylated p65 (pp65) (9687), Akt1 (4691), phosphorylated Akt1 (pAkt1) (4060), p38 (8690), phosphorylated p38 (pp38) (4511), p44/42 (4695), phosphorylated p44/42 (pp44/42) (9101), β-actin (7076), and the corresponding horseradish peroxidase-conjugated secondary antibodies (7074). Protein bands were visualized using a western blotting substrate (Thermo Fisher Scientific). β-actin served as the reference protein.

Quantitative PCR: Total RNA was isolated from cells using the RNeasy mini kit (Qiagen, Germantown, MD, USA). qPCR was performed in a CFX System (Bio-Rad, Hercules, CA, USA) for 40 cycles. Primers were designed as follows; 5′-CCAGAGATTCGCAAACCAGAGG-3′ (caspase-9 forward), 5′-ATGGACACCTTCTTGGACGACAG-3′ (APAF forward), 5′-GATTGATGGGATCGTTGCCTTA-3′ (Bcl-2 forward), 5′-GAACCATCATGGGCTGGACA-3′ (Bax forward), 5′-ATCATCTTCTCGAACCCCGA-3′ (TNF-α forward), 5′-GTTATCTCTCAGCTCCACGC-3′ (TNF-α reverse), 5′-AGCTCGCCAGTGAAATGATG-3′ (IL-1β forward), 5′-CGGAGATTCGTAGCTGGATG-3′ (IL-1β reverse), 5′-ACTCACCTCTTCAGAACGAATTG-3′ (IL-6 forward), 5′-CCATCTTTGGAAGGTTCAGGTTG-3′ (IL-6 reverse), 5′-GGGGACAGAGTTCATGTGGT-3′ (IL-17 forward), 5′-CCACCTCACCTTGGAATCTC-3′ (IL-17 reverse), 5′-TTCAGTATCACAACCTCAGCAAG-3′ (iNOS forward), 5′-TGGACCTGCAAGTTAAAATCCC-3′ (iNOS reverse), 5′-CCTGCCTAACATGCTTCGAG-3′ (IL-10 forward), 5′-GTCTTGGTTCTCAGCTTGGG-3′ (IL-10 reverse), 5′-GACTCGCCAGAGTGGTTATC-3′ (TGF-β forward), 5′-GGTAGTGAACCCGTTGATGT-3′ (TGF-β reverse), 5′-TGCACCACCAACTGCTTAGC-3′ (glyceraldehyde 3-phosphate dehydrogenase (GAPDH) forward), and 5′-GGCATGGACTGTGGTCATGAG-3′ (GAPDH reverse). Quantification was performed by using the 2−ΔΔCT method normalizing to the control for percent fold changes.

Antimigratory Effect: For the invasion assay, A549 cells (5×10^6 cells per well) were seeded onto Matrigel-coated polycarbonate membrane inserts (Thermo Fisher Scientific) in 24-well plates. Cells were treated with REVs at final concentrations of 10, 20, and 30 μg mL^{-1}. After incubation for 24 h, noninvasive cells on the upper membrane of the insert were removed, and invasive cells on the lower membrane of the insert were stained with crystal violet. For the migration assay, A549 cells (5×10^5 cells per well) were seeded in a culture insert within a μ-dish (35 mm, Ibidi, Fitchburg, WI, USA) and grown at 95% confluence. The inserts were then removed, and cells were treated with REVs at 10, 20, and 30 μg mL^{-1} ($n = 5$). Representative images were captured at 0 and 24 h to compare migratory efficiency, and wound closure rates were quantified using ImageJ.

Tumor Targeting and Photothermal Activities: Male BALB/c nude mice (6–7 weeks old) were purchased from Japan SLC Inc. All animal studies were approved by the regulations of the Institutional Animal Care and Use Committee of the Korea Research Institute of Bioscience and Biotechnology, in compliance with ethical standards and to minimize animal suffering. Mice were subcutaneously (s.c.) inoculated with A549 cells (5×10^6 cells in 20 μL PBS) in the right back of the hind leg region. When the tumors reached a volume of 100 mm^3, free ICG and REV-ICG were administrated i.v., i.p., or p.o. at a dose of 5 mg kg^{-1}. Mice were anesthetized and imaged using an in vivo fluorescence imaging system (IVIS, Xenogen, San Francisco, CA, USA) 24 h after REV-ICG administration. For ex vivo fluorescence imaging, mice were sacrificed 24 h post-injection, and tumors, along with major organs (liver, heart, lung, spleen, and kidney), were collected and imaged using the IVIS system. To evaluate the photothermal activity of REV-ICG, tumors were exposed to a NIR laser (1 W cm^{-2}) 24 h post-injection of REV-ICG. Thermal images were captured at 0, 2, 4, and 5 min using a thermal camera.

Anti-tumor Activity: To establish a xenograft mouse model, A549 cells (5×10^6 cells in 20 μL PBS) were s.c. Implanted into the right flank of 6–7 week-old BALB/c mice. Once tumors reached ≈30 mm^3, mice were randomly divided into groups and treated with free ICG, REVs, and REV-ICG (5 mg kg^{-1} in 100 μL PBS, $n = 5$) via three different three routes, p.o., i.p., and i.v. For i.p. and i.v. administrations, and treatments were given on days 0, 2, 4, 7, 9, and 11. For p.o. administration, the treatments were administered on days 0, 1, 2, 3, 4, 7, 8, 9, 10, and 11. Tumor sites were exposed to an NIR laser (1 W cm^{-2}) for 5 min on days 7 and 14. Tumor temperature changes were monitored using a thermal camera. Tumor sizes were measured every 2 days for 30 days and calculated using the following formula: tumor volume (V) = 1/2 × length (mm) × width (mm)^2. On day 32, mice were euthanized, and the tumors were harvested and weighed. For survival analysis, mice were monitored for 90 days and euthanized if their tumor volume reached ≈1000 mm^3.

Histological Evaluation: Tumor tissues were harvested on day 32 and fixed with 4% formaldehyde (Thermo Fisher Scientific). Paraffin-molded tumor tissues were sliced to 7 μm and stained with hematoxylin and eosin (H&E), TUNEL (Promega), anti-Ki67 (1:200, Invitrogen, Waltham, MA, USA), anti-CD31 (1:500, Invitrogen), anti-CRT (1:500, Invitrogen), and anti-HMGB1 (1:1000, Cell Signaling Technology, MA, USA) followed by appropriate secondary antibodies, labeled with FITC and Alexa Fluor 594, respectively. Nuclei were visualized with DAPI. Fluorescent images were acquired using a CLSM and fluorescent intensities were quantified using an ImageJ program.

In Vivo Pharmacokinetics: Nude BALB/c mice were treated with REV-ICG (5 mg kg^{-1} in 100 μL PBS, $n = 5$) via p.o., i.p., and i.v. administration routes. Blood samples were collected at various time points (0, 1, 3, 5, 8, and 24 h) and centrifuged at 500 g for 5 min to isolate plasma. The concentration of REV-ICG in the plasma samples was measured using a microplate reader at an absorption wavelength of 800 nm. Pharmacokinetic parameters, including the AUC and maximum concentration (C_{max}), were calculated using GraphPad Prism software. The AUC was determined using the trapezoidal method, integrating concentration-time curves from 0 to 24 h. C_{max} was directly obtained from the observed concentration-time data (Y-Axix values).

Biosafety Evaluation: At the end point of the in vivo experiment on day 32, blood samples and major organs were harvested. The organs, including the liver, heart, lung, spleen, and kidney, were fixed, sectioned, and stained with H&E for histological examination. Serum biomarkers were evaluated to determine hepatic and renal toxicities. The levels of ALT and AST were measured as hepatic markers, while ALB and CRE were measured as renal markers, using each commercial kit (Abcam, UK), following manufacturer protocols.

Statistical Analysis: All data from the characterization of REVs (or REV-ICG), in vitro, and in vivo studies were analyzed in GraphPad Prism v8 and are presented as mean ± standard deviations. Statistical significance was determined using one-way analysis of variance (ANOVA) with a post hoc Tukey's HSD test for multiple comparisons and Student's t-test for pairwise comparison. Statistical significance for mice survival was determined using the log-rank (Mantel-Cox) test. Statistical significance was considered when $p < 0.05$ and defined as $^*p < 0.05$, $^{**}p < 0.01$, and $^{***}p < 0.001$.

Supporting Information

Supporting Information is available from the Wiley Online Library or from the author.

Acknowledgements

S.Y. and E.J. contributed equally to this work. This research was supported by NRF and NST grants funded by Korea government (MSIT) (2021M3H4A1A02051048, 2023R1A2C2005185, 2021M3E5E3080844, 2022R1C1C1008815, RS-2024-00348576, RS-2024-00438316, and RS-2024-00459749), KEIT grants funded by Korea government (MOTIE) (RS-2022-00154853, RS-2024-00403563, and RS-2024-00432382), KEITI grant funded by Korea government (ME) (2021003370003), IPET grant funded by Korea government (MAFRA) (RS-2024-00401639), Nanomedical Devices Development Program of National Nano Fab Center, and KRIBB Research Initiative Program (KGM1322511 and KGM1032511). [Correction added on March 12, 2025, after first online publication: Funding number of KRIBB Research Initiative Program in the Acknowledgement Section has been updated.]

Conflict of Interest

The authors declare no conflict of interest.

Data Availability Statement

The data that support the findings of this study are available in the supplementary material of this article.

Keywords

drug delivery platforms, extracellular vesicles, oral administration, photothermal therapy, probiotics

Received: July 19, 2024
Revised: October 9, 2024
Published online: October 18, 2024

[1] D. Zheng, H. Ruan, W. Chen, Y. Zhang, W. Cui, H. Chen, H. Shen, *Bioact. Mater.* **2023**, *25*, 500.
[2] a) F. Kolonics, V. Szeifert, C. I. Timar, E. Ligeti, A. M. Lorincz, *Cells* **2020**, 9; b) S. Hallal, A. Tuzesi, G. E. Grau, M. E. Buckland, K. L. Alexander, *J. Extracell. Vesicles* **2022**, *11*, e12260; c) S. Ghadami, K. Dellinger, *Front. Mol. Biosci.* **2023**, *10*, 1198044.
[3] a) M. P. Zaborowski, L. Balaj, X. O. Breakefield, C. P. Lai, *Bioscience* **2015**, *65*, 783; b) S. Gurung, D. Perocheau, L. Touramanidou, J. Baruteau, *Cell Commun. Signal* **2021**, *19*, 47; c) Y. Hao, H. Song, Z. Zhou, X. Chen, H. Li, Y. Zhang, J. Wang, X. Ren, X. Wang, *J. Control Rel.* **2021**, *340*, 136; d) C. Chen, H. Zheng, Y. Luo, Y. Kong, M. An, Y. Li, W. He, B. Gao, Y. Zhao, H. Huang, J. Huang, T. Lin, *J. Clin. Invest.* **2021**, 131.
[4] a) E. I. Buzas, *Nat. Rev. Immunol.* **2023**, *23*, 236; b) Z. Zhi, Q. Sun, W. Tang, *Front. Mol. Biosci.* **2022**, *9*, 1036746.
[5] a) A. Y. Jong, C. H. Wu, J. Li, J. Sun, M. Fabbri, A. S. Wayne, R. C. Seeger, *J. Extracell Vesicles* **2017**, *6*, 1294368; b) L. Zhu, P. Gangadaran, S. Kalimuthu, J. M. Oh, S. H. Baek, S. Y. Jeong, S. W. Lee, J. Lee, B. C. Ahn, *Artif. Cells Nanomed. Biotechnol.* **2018**, *46*, 166; c) A. L. Di Pace, N. Tumino, F. Besi, C. Alicata, L. A. Conti, E. Munari, E. Maggi, P. Vacca, L. Moretta, *Cancers* **2020**, 12; d) J. W. Choi, S. Lim, J. H. Kang, S. H. Hwang, K. C. Hwang, S. W. Kim, S. Lee, *Molecules* **2020**, 25; e) L. Zhu, S. Kalimuthu, P. Gangadaran, J. M. Oh, H. W. Lee, S. H. Baek, S. Y. Jeong, S. W. Lee, J. Lee, B. C. Ahn, *Theranostics* **2017**, *7*, 2732.
[6] a) H. Hao, X. Zhang, L. Tong, Q. Liu, X. Liang, Y. Bu, P. Gong, T. Liu, L. Zhang, Y. Xia, L. Ai, H. Yi, *Front. Immunol.* **2021**, *12*, 777147; b) F. Han, K. Wang, K. Shen, J. Wang, S. Han, D. Hu, G. Wu, *J. Nanobiotechnol.* **2023**, *21*, 113; c) J. A. Molina-Tijeras, J. Galvez, M. E. Rodriguez-Cabezas, *Nutrients* **2019**, 11; d) Y. Shi, L. Meng, C. Zhang, F. Zhang, Y. Fang, *Microbiol. Res.* **2022**, *259*, 126955.
[7] J. Escamilla, M. A. Lane, V. Maitin, *Nutr. Cancer* **2012**, *64*, 871.
[8] a) X. Kang, H. C. Lau, J. Yu, *Cell Rep. Med.* **2024**, *5*, 101478; b) A. Garczyk, I. Kaliciak, K. Drogowski, P. Horwat, S. Kopec, Z. Starega, P. Bogdanski, M. Stelmach-Mardas, M. Mardas, *J. Clin. Med.* **2022**, 11; c) Z. Juan, J. Chen, B. Ding, L. Yongping, K. Liu, L. Wang, Y. Le, Q. Liao, J. Shi, J. Huang, Y. Wu, D. Ma, W. Ouyang, J. Tong, *Eur. J. Cancer* **2022**, *161*, 10.
[9] L. Tripodi, S. Feola, I. Granata, T. Whalley, M. Passariello, C. Capasso, L. Coluccino, M. Vitale, G. Scalia, L. Gentile, C. De Lorenzo, M. R. Guarracino, G. Castaldo, V. D'Argenio, B. Szomolay, V. Cerullo, L. Pastore, *iScience* **2023**, *26*, 107668.
[10] Z. Yang, Z. Gao, Z. Yang, Y. Zhang, H. Chen, X. Yang, X. Fang, Y. Zhu, J. Zhang, F. Ouyang, J. Li, G. Cai, Y. Li, X. Lin, R. Ni, C. Xia, R. Wang, X. Shi, L. Chu, *Pharmacol. Res.* **2022**, *182*, 106332.
[11] R. Sanwlani, L. Gangoda, *Cells* **2021**, 10.
[12] T. H. Baryakova, B. H. Pogostin, R. Langer, K. J. McHugh, *Nat. Rev. Drug Discov.* **2023**, *22*, 387.
[13] A. Latif, A. Shehzad, S. Niazi, A. Zahid, W. Ashraf, M. W. Iqbal, A. Rehman, T. Riaz, R. M. Aadil, I. M. Khan, F. Ozogul, J. M. Rocha, T. Esatbeyoglu, S. A. Korma, *Front. Microbiol.* **2023**, *14*, 1216674.
[14] R. Hu, H. Lin, M. Wang, Y. Zhao, H. Liu, Y. Min, X. Yang, Y. Gao, M. Yang, *J. Anim. Sci. Biotechnol.* **2021**, *12*, 25.
[15] a) C. Zheng, M. Zheng, P. Gong, D. Jia, P. Zhang, B. Shi, Z. Sheng, Y. Ma, L. Cai, *Biomaterials* **2012**, *33*, 5603; b) C. W. Ting, Y. H. Chou, S. Y. Huang, W. H. Chiang, *Colloids Surf B Biointerfaces* **2021**, *208*, 112048.
[16] H. Wang, X. Li, B. W. Tse, H. Yang, C. A. Thorling, Y. Liu, M. Touraud, J. B. Chouane, X. Liu, M. S. Roberts, X. Liang, *Theranostics* **2018**, *8*, 1227.
[17] a) M. Redza-Dutordoir, D. A. Averill-Bates, *Biochim. Biophys. Acta.* **2016**, *1863*, 2977; b) L. Covarrubias, D. Hernandez-Garcia, D. Schnabel, E. Salas-Vidal, S. Castro-Obregon, *Dev. Biol.* **2008**, *320*, 1.
[18] a) T. Park, S. Lee, R. Amatya, H. Cheong, C. Moon, H. D. Kwak, K. A. Min, M. C. Shin, *Int. J. Nanomed.* **2020**, *15*, 5459; b) N. Kwon, G. O. Jasinevicius, G. Kassab, L. Ding, J. Bu, L. P. Martinelli, V. G. Ferreira, A. Dhaliwal, H. H. L. Chan, Y. Mo, V. S. Bagnato, C. Kurachi, J. Chen, G. Zheng, H. H. Buzza, *Angew. Chem. Int. Ed. Engl.* **2023**, *62*, 202305564.
[19] a) P. Xu, F. Liang, *Int. J. Nanomed.* **2020**, *15*, 9159; b) D. V. Krysko, A. D. Garg, A. Kaczmarek, O. Krysko, P. Agostinis, P. Vandenabeele, *Nat. Rev. Cancer* **2012**, *12*, 860.
[20] a) X. Li, X. Li, B. Zhang, B. He, *Stem Cells Int.* **2022**, *2022*, 9133658; b) J. Yang, Y. Teng, *J. Exp. Clin. Cancer Res.* **2023**, *42*, 131.
[21] a) A. Sarasati, M. H. Syahruddin, A. Nuryanti, I. D. Ana, A. Barlian, C. H. Wijaya, D. Ratnadewi, T. D. K. Wungu, H. Takemori, *Biomedicines* **2023**, 11; b) N. Mu, J. Li, L. Zeng, J. You, R. Li, A. Qin, X. Liu, F. Yan, Z. Zhou, *Int. J. Nanomed.* **2023**, *18*, 4987.
[22] a) M. Samuel, P. Fonseka, R. Sanwlani, L. Gangoda, S. H. Chee, S. Keerthikumar, A. Spurling, S. V. Chitti, D. Zanker, C. S. Ang, I. Atukorala, T. Kang, S. Shahi, A. L. Marzan, C. Nedeva, C. Vennin, M. C. Lucas, L. Cheng, D. Herrmann, M. Pathan, D. Chisanga, S. C. Warren, K. Zhao, N. Abraham, S. Anand, S. Boukouris, C. G. Adda, L. Jiang, T. M. Shekhar, N. Baschuk, et al., *Nat. Commun.* **2021**, *12*, 3950; b) L. Zhang, S. Li, M. Cong, Z. Liu, Z. Dong, M. Zhao, K. Gao, L. Hu, H. Qiao, *Nano Lett.* **2023**, *23*, 1555; c) W. Zhang, Y. Yuan, X. Li, J. Luo, Z. Zhou, L. Yu, G. Wang, *Front. Immunol.* **2022**, *13*, 900963.
[23] a) Y. Li, T. Ji, M. Torre, R. Shao, Y. Zheng, D. Wang, X. Li, A. Liu, W. Zhang, X. Deng, R. Yan, D. S. Kohane, *Nat. Commun.* **2023**, *14*, 6659; b) Y. Okamoto, K. Taguchi, K. Yamasaki, M. Sakuragi, S. Kuroda, M. Otagiri, *J. Pharm. Sci.* **2018**, *107*, 436.
[24] K. Kuerban, X. Gao, H. Zhang, J. Liu, M. Dong, L. Wu, R. Ye, M. Feng, L. Ye, *Acta Pharm. Sin. B.* **2020**, *10*, 1534.

